Arabian Journal of Chemistry (2022) **15**, 103904

King Saud University

Arabian Journal of Chemistry

www.ksu.edu.sa
www.sciencedirect.com

ORIGINAL ARTICLE

Hierarchically porous tobacco midrib-based biochar prepared by a simple dual-templating approach for highly efficient Rhodamine B removal

Xinyu Zhang [a], Tingwei Zhang [a,*], Jiaqi Guo [a], Mehraj Ahmad [a], Hui Yang [b], Xiankun Su [b], Feng Huang [c], Yongcan Jin [a], Huining Xiao [d], Junlong Song [a,*]

[a] *International Innovation Center for Forest Chemicals and Materials and Jiangsu Co-Innovation Center for Efficient Processing and Utilization of Forest Resources, Nanjing Forestry University, Nanjing 210037, China*
[b] *Guizhou Academy of Tobacco Science, Guiyang 550081, China*
[c] *Zhengzhou Tobacco Research Institute of CNTC, Zhengzhou 450001, China*
[d] *Department of Chemical Engineering, University of New Brunswick, Fredericton, NB E3B 5A3, Canada*

Received 23 February 2022; accepted 4 April 2022
Available online 09 April 2022

KEYWORDS

Biochar;
Activation;
Adsorption;
Rhodamine B;
Thermodynamics

Abstract High volatile matter contents in the feedstock could promote the development of porous structures and the reactivity of biochar. Herein, tobacco midrib with high volatile matter contents was used to prepare biochar by a dual-templating approach with mild activators ($K_2C_2O_4{\cdot}H_2O$, $CaCO_3$). The characterizations of textural properties indicated that tobacco midrib-based biochar possessed numerous meso-, micro-, and macro-pores, specific surface area reached 1841.9 $m^2\ g^{-1}$. As a dye adsorbent, the adsorption capacity of this biochar towards Rhodamine B reached 588.7 mg g^{-1}. After recycling 5 times, it still retained over 90% of its initial adsorption capacity. Moreover, thermodynamic parameters assessed with full vaṅt Hoff equation confirmed that dye molecules replace water molecules connected on biochar surface during the adsorption according to negative heat capacity change (-3.9 kJ $mol^{-1}\ K^{-1}$), ΔH^0 (–22.1 kJ mol^{-1}) and ΔS^0 (0.3 kJ mol^{-1}) revealed that the adsorption process of Rh B by TMB was exothermic and the disorder of the

* Corresponding authors.
E-mail addresses: zhangxinyu4391@163.com (X. Zhang), ztwei@njfu.edu.cn (T. Zhang), jiaqi.guo@njfu.edu.cn (J. Guo), mehraajk@gmail.com (M. Ahmad), yanghui11111@126.com (H. Yang), 65613687@qq.com (X. Su), huangf004@163.com (F. Huang), jinyongcan@njfu.edu.cn (Y. Jin), hxiao@unb.ca (H. Xiao), junlong.song@njfu.edu.cn, ztwei@njfu.edu.cn, junlong.song@gmail.com, junlong.song@njfu.edu.cn (J. Song).
Peer review under responsibility of King Saud University.

ELSEVIER Production and hosting by Elsevier

https://doi.org/10.1016/j.arabjc.2022.103904

solid–liquid interface increased. Overall, this research provides a mild and effective approach to modifying biochar from special tissue of agriculture waste and an insight into the process of dye adsorption on biochar from thermodynamics.

1. Introduction

Some pigments in wastewater can severely damage aquatic ecosystems and have serious effects on humans, such as allergies, cancer, mutations, and so on (Godiya et al. 2020; Lin et al. 2020; Soliman et al. 2022). Now various techniques including adsorption, membrane filtration, and advanced oxidation processes (like Fenton, electrocatalysis, ozone, and electrochemical oxidation) have been extensively used for the removal of dyes from wastewater environment (Jalili Naghan et al. 2015; Albadarin et al. 2017; Boudissa et al. 2019; Crini and Lichtfouse 2019). Among them, adsorption technology could be effectively used for the removal of pollutants without producing toxic byproducts from wastewater (Wang and Wang 2019; Xiang et al. 2020; Huang et al. 2021; Liu et al. 2021; Abdelhamid and Mathew 2022).

Biochar has been applied as an adsorbent in removal of water pollutants in recent years (Huang et al. 2019; Hu et al. 2020). A lot of agricultural wastes are used to generate biochar including bagasse, banana skin, walnut shell, coconut shell, etc. (Tonucci et al. 2015; Gupta and Gupta 2016; Rattanachueskul et al. 2017; Tang et al. 2017; Paunovic et al. 2019). In China, the tobacco planting area under cultivation is more than 10 million hectares (Hu et al. 2015). During tobacco harvesting and leaf processing, huge quantities of by-products and wastes are discarded. Tobacco biomass waste being a rich carbon source is composed of cellulose, hemicellulose, and lignin (Wei et al. 2020). It could be processed and converted into tobacco biochar for wastewater treatment. Tobacco stem is used to prepare biochar as adsorbents to remove pollutants (Mudyawabikwa et al. 2017; Zhou et al. 2018). But now no studies on the use of tobacco midrib for biochar preparation. The midrib is the primary vein that extends off from the stalk and is removed during the processing of the tobacco leaf. Some aroma compounds, viz. nicotine present in the midrib usually return to the process for the development of low-quality products or are used as basic materials for the extraction of volatile organic compounds (Banozic et al. 2020). Compared with the stem, the midrib is mainly composed of vessels rather than fiber cell walls. The cell wall is mainly lignin and cellulose based macromolecules with strong structure, while cellulose and small molecule volatiles in vessels. Therefore, it is rational to hypothesize that a much tender activation is required for midrib biochar activation. The green conversion of agricultural wastes to biochar is significant for environmental sustainability.

In general, for carbon-based adsorbents, surface area, pore size distribution, and functional groups have a great effect on adsorption capacity (Pereira et al. 2003; Wang and Wang 2019). The chemical activation is often used to modulate the properties of biochar for increasing the specific surface area (S_{BET}) of biochar to improve adsorption capacity. The strong bases (sodium hydroxide, potassium hydroxide), acids (phosphoric acid), and metal salts (zinc chloride) were commonly used as chemical activators (Bedin et al. 2016; Lee et al. 2018; Xu et al. 2020). The disadvantages are that strong acid or alkali activators tend to damage equipment and require a prolonged process for impregnation and drying (Shi et al. 2021). Also, the activators are not conducive to adjusting pore size, which determines the accessibility of the active sites and mass transfer limitation (You et al. 2017). The template-based method is another effective approach for the synthesis of carbon materials with well-controlled *meso*-pores. For the carbonization of raw lignocelluloses with recalcitrant structure, the templates are rarely interacted with carbon precursors, resulting in poor effect in pore-forming (Liang et al. 2008; Li et al. 2019). The dual-templating approach takes advantage of the accurate replication of pore structure, and also ensures the adjustment of *meso*-pore structure, thus obtaining hierarchical porous carbon materials with higher controllability of pore structure and surface morphology (Sevilla et al. 2017).

High volatile matter contents in the feedstock could promote the development of porous structures and the reactivity of biochar (You et al. 2017). Until now, on the one hand, the influence of the varied compositions from tobacco biomasses is not reported; on the other hand, adsorption capacity of biochar modified with the dual-templating approach is not clear. Herein, tobacco midrib and tobacco stem biochars were produced by using a simple dual-templating approach with mild activators ($K_2C_2O_4{\cdot}H_2O$, $CaCO_3$). Rhodamine B (Rh B) was chosen for assessing the performance of biochar in removing the dye from aqueous solutions. The effects of pH medium, biochar dosage, adsorption temperature, adsorption kinetics, and isotherms on the adsorption were investigated to reveal the adsorption behaviors. A negative change of heat capacity for the adsorption of dye on biochar was observed for the first time using the full vanť Hoff equation.

2. Experimental

2.1. Materials

Tobacco midrib (TM) and tobacco stem were provided by Zhengzhou Tobacco Research Institute of CNTC (China National Tobacco Company, Zhengzhou, China). Rhodamine B (Rh B, Mw = 479.01 g mol^{-1}) and potassium oxalate monohydrate ($K_2C_2O_4{\cdot}H_2O$) were procured from Aladdin Bio-Chem Technology Co., Ltd (Shanghai, China). Hydrogen chloride (HCl, 36.7 wt%), Sodium hydroxide (NaOH), and Calcium carbonate ($CaCO_3$) were obtained from Sinopharm Chemical Reagent Co., Ltd. (Shanghai, China). Ethanol (99.5 wt%) was acquired from Yasheng Chemical Co., Ltd (Wuxi, China). All solutions used in this study were prepared from distilled/deionized water (resistivity $\sim$ 18.2 MΩ·cm).

2.2. Preparation of biochar samples

Briefly, the grinded tobacco midrib was heated at 600 °C for 1 h with a heating rate of 5 °C min^{-1} under N_2 atmosphere at a flow rate of 40 mL min^{-1} in a tube furnace (Kejing, GSL-1100X-XX-S2). The sample was subjected to pre-carbonization to enhance thermal stability. After that, simultaneously adding $K_2C_2O_4{\cdot}H_2O$, and $CaCO_3$ into the pre-carbonized biochar (PCB) samples (mass ratio 1: 1: 1) were mixed uniformly (Sevilla et al. 2017). The mixture was grinded and then calcined at 800 °C for 1 h at a 3 °C min^{-1} heating rate in a tube furnace under N_2 flow as mentioned above. The sample obtained was dispersed in 2 mol L^{-1} HCl solution for several hours. The pH of the mixture was neutralized before washing. At last, TMB was filtered off using a Buchner funnel followed by drying at 80 °C for 8 h using the oven (DHG, Shanghai, China). As a comparison, tobacco midrib carbon (TMC) was prepared without activators under the same conditions. Another raw material, tobacco stem was used to prepare tobacco stem biochar (TSB) by the same method. The schematic representation of preparation of TMB was illustrated in Scheme 1.

2.3. Characterization

Thermogravimetric analysis (TGA) was conducted on a thermal analyzer TGA209 F1 (Netzsch, Germany) at the heating rate of 5 °C min^{-1}. The samples were tested in the temperature range of 20 to 800 °C under N_2 atmosphere (flow rate about 20 mL min^{-1}). The surface morphology was visualized through a scanning electron microscope (SEM, JSM-7600F). The crystalline structure and diffraction patterns of the samples were analyzed through X-ray diffraction (XRD, Rigaku Ultima IV). Diffraction data were taken in the 2θ range of 10 to 80° at a scan rate of 10° min^{-1}. The functional groups of the samples were analyzed by Fourier transform infrared spectroscopy (FT-IR) on VERTEX 80 V, which were recorded using 1 wt% of the sample in KBr tablet under ambient conditions. The surface compositions of samples were determined on an Ultra DLD X-ray photoelectron spectrometer (XPS) fitted with a hemispherical analyzer and a conventional monochromatic Al Ka X-ray source. The textural properties of the samples were evaluated via N_2 adsorption–desorption experiments using a surface area analyzer (QuantaChrome Nova 1200). S_{BET} was calculated by using the Brunauer-Emmett-Teller equation and pore size distribution was calculated by using the density functional theory model, micropore surface area and external surface area were evaluated by the *t*-plot method.

The point of zero charge (pH_{pzc}) was determined by a solid additional method (Mena-Durán et al. 2018).

The concentration of Rh B was determined through the spectrophotometric method using a double beam UV–Visible spectrophotometer (Shimadzu, UV-1780) at 554 nm wavelength. The standard curve for Rh B was shown in Fig. S1. The Rh B concentration was calculated according to Eq. (1).

$$C = (A - 0.0038)/0.2140 \quad (1)$$

where C (mg L^{-1}) is the concentration of Rh B, A is the absorbance of the sample solution.

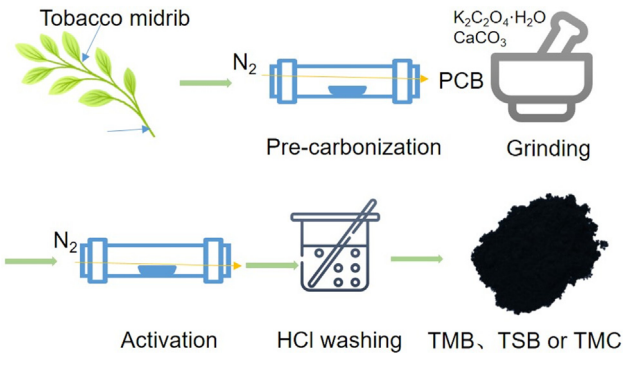

Scheme 1 Schematic representation of preparation of TMB.

2.4. Adsorption experiments

The desired amount of TMB sample was mixed with 100.0 mL of Rh B solution in a 250 mL glass jar using an incubator shaker (ZWY-2101, Shanghai, China) at a constant stirring (150 rpm). The effects of various adsorption parameters viz. initial pH of Rh B solution (2.0–12.0), absorbent dosage (5.0–25.0 mg), contact time (1–40 min), Rh B concentration (50.0–200.0 mg L^{-1}), and adsorption temperature (25.0, 40.0, and 55.0 °C) were investigated. After adsorption analysis, the recovered TMB was recycled by washing with ethanol (Liu et al. 2019). Then the recycled TMB was tested for dye removal performance by following similar steps to the adsorption experiments.

For the kinetic analysis, the as-prepared TMB was thoroughly mixed with different Rh B solutions and then shaken for various designed periods.

The dye removal and adsorption capacity (q_t), as defined by Eqs., respectively.

$$\text{Removal} = (C_0 - C_e)/C_0 * 100\% \quad (2)$$

$$q_t = (C_0 - C_t)V/m \quad (3)$$

where C_0 and C_t are initial Rh B concentration and concentration at time t (mg L^{-1}), respectively; q_t is the adsorption amount of the adsorbent at time t (mg g^{-1}); m and V are TMB mass (g) and Rh B solution volume (L), respectively.

2.5. Adsorption kinetics and adsorption isotherm models

The pseudo-first-order and pseudo-second-order were used to analyze adsorption kinetics (Azari et al. 2021)(4, 5). Langmuir and Freundlich isotherm models were used in this study (6, 7).

$$q_t = q_e[1 - \exp(-k_1 t)] \quad (4)$$

$$q_t = \frac{k_2 q_e^2 t}{1 + k_2 q_e t} \quad (5)$$

where q_e represents the equilibrium adsorption amount of Rh B adsorbed (mg g^{-1}), k_1 (min^{-1}) and k_2 (g mg^{-1} min^{-1}) are the adsorption rate constant for pseudo-first-order and pseudo-second-order, respectively.

$$q_e = \frac{q_m K_L C_e}{1 + K_L C_e} \quad (6)$$

$$q_e = K_f C_e^{\frac{1}{n}} \quad (7)$$

q_m: the maximum adsorption amount of Rh B (mg g^{-1}); K_L is the adsorption equilibrium constant of Langmuir isotherm; K_f: the Freundlich constant associated with the adsorption capacity (mg $L^{1/n}$ g^{-1}); n: the adsorption intensity of the adsorbent.

The contribution of Gibbs free energy change (ΔG^0), enthalpy change (ΔH^0), entropy change (ΔS^0), and heat capacity change (ΔC_p) to the adsorption of Rh B on TMB was discussed by using the full vant Hoff equation (Liu et al. 2020).

$$\Delta G^0 = -RT\ln K_e \quad (8)$$

$$\ln K_e = \frac{-\Delta Ho(T0)}{RT} + \frac{-\Delta S0(T0)}{R} + \frac{\Delta Cp}{R}\left[\left(\frac{T-T0}{T}\right) - ln\frac{T}{T0}\right] \quad (9).$$

$$\Delta G^0 = \Delta H^0 - T\Delta S^0 \quad (10)$$

$$K_e \approx K_L(L/momol) \times C_0(mol/L) \times 10^3 \quad (11)$$

where T (K) is the thermodynamic equilibrium constant, R is the gas constant (8.314 J K^{-1} mol^{-1}).

3. Results and discussion

3.1. Characteristics of samples

In Fig. 1, the surface of the PCB of tobacco midrib and stem was smooth and flat without visible pore structure shown in Fig. 1(a, c), while TMB and tobacco stem biochar surface possess pores structure after the activation. In particular, many large and small pores appeared on the surface of TMB. TM contains a large number of volatile substances, and the components are looser than the stem. The activation could dramatically improve the porosity of the PCB. $K_2C_2O_4{\cdot}H_2O$ as a soft template while $CaCO_3$ as a hard template could synthesize hierarchically porous materials effectively. In the activation process, both $K_2C_2O_4{\cdot}H_2O$ and $CaCO_3$ could be hydrolyzed along with the release of CO_2 gas in calcination during the thermal treatment. This could be associated with the activation of dormant pores and the formation of micropores on PCB. In addition, CO could release *in situ* due to redox reactions of carbon with K_2CO_3 and/or evolved CO_2 (Sevilla et al. 2017). Owing to the dual-templating approach, a carbon material with an open macroporous (improved mass transfer capacity) and foam-like hierarchical pore structure rich in micro-/*meso*-pores is successfully achieved.

The results of textural properties collected at 77 K N_2 atmosphere were shown in Fig. 2(a and b). It showed an IV(a) type isotherm with an H4 hysteresis loop for TMB and TSB, suggesting the presence of finite mesoporosity along with slit pores (Bedin et al. 2016; Li et al. 2016). The S_{BET}, micropore area, and external surface area were shown in Table 1. An interesting result was noticed, the S_{BET} of TMC reached 341.6 m^2 g^{-1}, which was much higher than other biochar, like soybean cake biochar (Zhang et al. 2022), and rice straw biochar (Jiang et al. 2012), sludge-based biochar (Zhang et al. 2019). The reason may be that tobacco midrib contains a large number of volatile substances, volatiles evaporate and leave a pore structure during the carbonization process. The S_{BET} of TMB reached up to 1841.9 m^2 g^{-1}, which was five folds more than that of TMC prepared without activators. The total pore volume was 1.1 cm^3 g^{-1} and the average pore diameter was 2.3 nm, which was broadly in line with the pore size distribution plot. The above results verified the existence of the hierarchically porous structure of TMB, especially with abundant micro-and *meso*-pores (Landers et al. 2013). In a word, due to this special composition, tobacco midrib is a high-quality raw material for the preparation of biochar. Concerning N_2

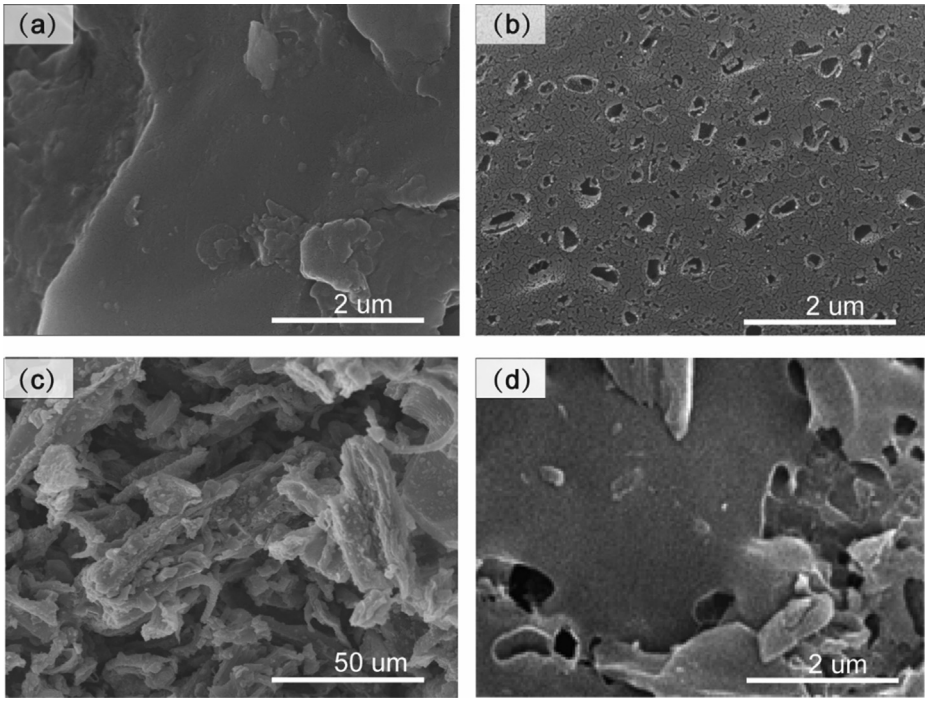

Fig. 1 SEM micrographs of (a) PCB, and (b) TMB, (c) tobacco stem pre-carbonization, (d) TSB.

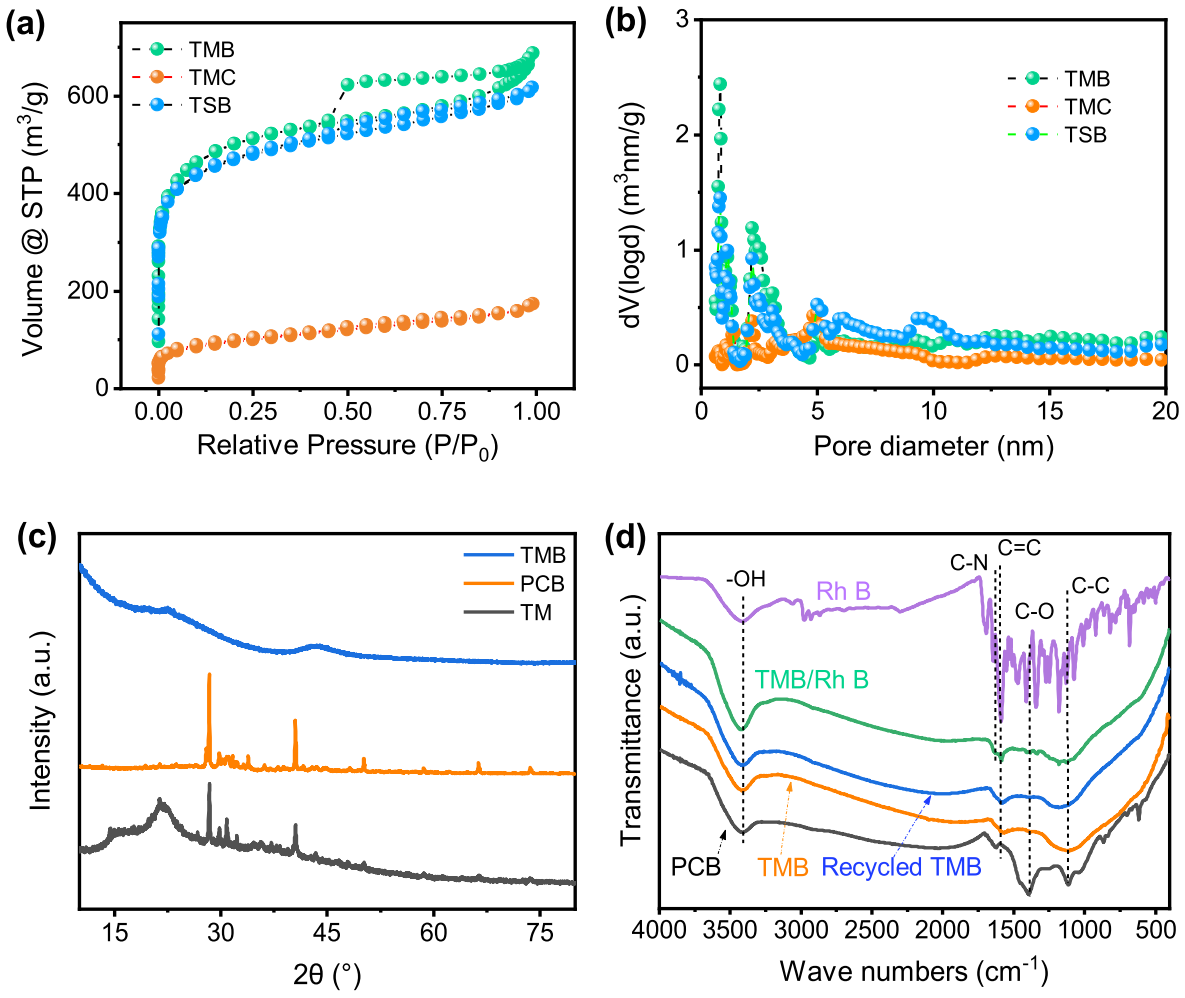

Fig. 2 N_2 adsorption–desorption isotherms (a) and pore size distribution (b) the XRD patterns (c), and FT-IR spectra for samples (d).

Table 1 The textural properties of samples.

Samples	Micropore area ($m^2\ g^{-1}$)	External surface area ($m^2\ g^{-1}$)	S_{BET} ($m^2\ g^{-1}$)	Average pore diameter (nm)	Total pore volume ($cm^3\ g^{-1}$)
TMC	149.8	191.8	341.6	1.4	0.2
TMB	1495.0	346.9	1841.9	2.3	1.1
TSB	1540.6	193.4	1734.0	2.2	0.9

adsorption–desorption results, the dual-templating approach is proved very effective in the activation of tobacco midrib biochar.

TM is mainly composed of cellulose, hemicelluloses, and lignin (as shown in Table S1). XRD pattern of TM was almost identical to that of cellulose because hemicelluloses and lignin are amorphous structures (Jin et al. 2016). The characteristic peak of $2\theta = 22.7°$ arising from the (002) plane of cellulose crystalline structure was noticeable in the TM, whereas this peak was disappeared in both biochar samples. After pre-carbonization, several new peaks appeared in the pattern of PCB due to the presence of inorganic substances in tobacco midrib raw material (Wu et al. 2015), $2\theta = 28.3, 40.5, 47.8, 50.1, 58.6, 66.3, 73.6$ reveal mineral sylvite (Pariyar et al. 2020). Nevertheless, the inorganic substances except biochar were completely washed away after HCl treatment as evidenced by the disappearance of weak peaks in the pattern of TMB. TMB is amorphous, as evidenced by the two typical broad diffraction peaks exhibited at 22.9° and 42.2° of graphitic carbon (Xiao et al. 2020).

In Fig. 2(d), broadbands at $\sim 3440\ cm^{-1}$ with strong intensity were observed in all samples due to the stretching vibration of the –OH group because of the presence of –OH or water molecules on the surface of the samples (Khan et al. 2019). In comparison with the spectra of TMB (before adsorption) and TMB/Rh B (TMB after Rh B adsorption), a prominent peak at $\sim 1640\ cm^{-1}$ has appeared for the latter, which corresponds to the stretching vibration of the C = N bond in Rh B. Besides, the peak at $1600\ cm^{-1}$, representing the stretching vibration of the aromatic ring for TMB, was shifted

some extent to 1617 cm^{-1} for TMB/Rh B due to the specific interaction.

The XPS spectra were shown in Fig. 3, three samples were mainly composed of C, and O; only slight content of N was shown in the pattern of TMB/Rh B due to the N species of Rh B structure. In Fig. 3(b), the C 1 s spectra were deconvoluted into four peaks, the strongest peak located at 284.8 eV was the characteristic peak of the C-C/C = C, and the other peaks at 285.8, 286.5, 287.5, and 288.9 eV corresponds to -C-OH, -C-O, -C = O, and -COOR functional groups, respectively (Mena-Durán et al. 2018; Wu et al. 2020; Ji and Li 2021). In Fig. 3(c), there were three peaks noticeable at 531.6, 532.8, and 534.3 eV representing O = C, O-C, and R-O-C = O, respectively (Wu et al. 2020). In Fig. 4(d), the N 1 s peaks are absent in TMB due to the lack of N; whereas some signals of N 1 s in TMB/Rh B were observed due to the presence of the N element in Rh B. Such a weak peak of N 1 s in recycled TMB was observed due to the trace residual dye, indicating that the used TMB could be washed clean enough by ethanol. The XPS spectra of the TMB and recycled TMB had almost identical characteristics, indicating that the adsorbent was stable during the adsorption and regeneration process.

3.2. Adsorption analysis

3.2.1. Effect of pH

The pH_{pzc} of TMB was shown in Fig. 4(a). The pH_{pzc} of TMB is determined to be about pH 5.3. Fig. 4(b) displays the relationship between the initial pH of Rh B solution and the removal efficiency using TMB. Maximum removal efficiency is observed at around pH 4. The structure and chemical nature of the adsorbent surface and dye are affected by the pH. The pK_a of –COOH is about 3.5–5.0. When the pH is < 3.5, the carboxyl groups on the surface of biochar are protonated, and the Rh B molecules are cationic forms as well. The cationic Rh B will replace the H sites in the oxygen-containing groups of the biochar during the adsorption process. When the pH value was 4, between 3.5 and 5.0, the carbonyl groups mainly exist as –COOH. The presence of –COOH facilitates the formation of hydrogen bonding between Rh B molecules and biochar, resulting in the improvement of Rh B adsorption. With the further increase of solution pH, the carboxyl groups were gradually ionized and formed $–COO^-$. The electrostatic attraction between the $–COO^-$ and biochar reduces resulting in a decrease in Rh B adsorption (Wang et al. 2017). While

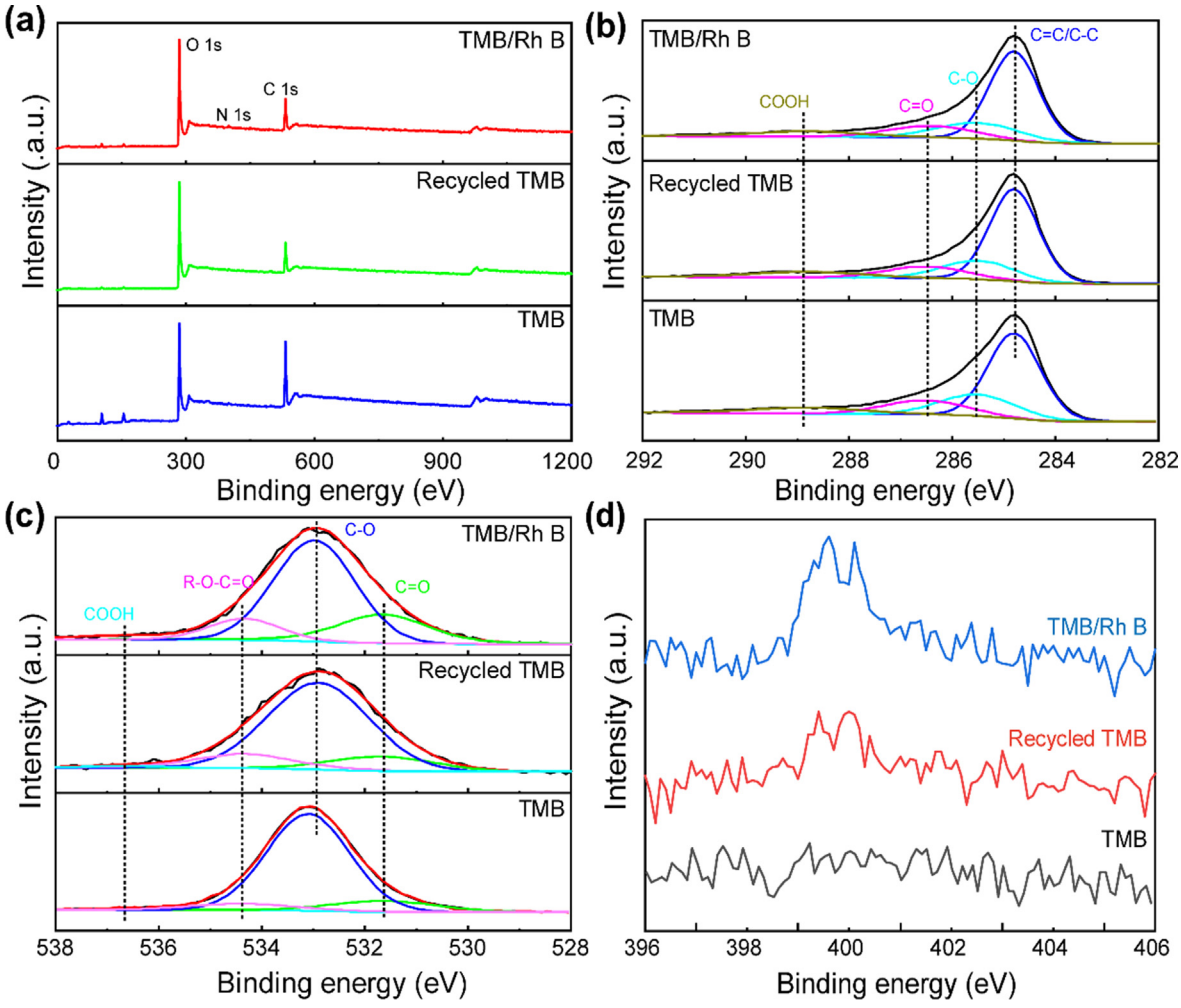

Fig. 3 XPS (a) wide patterns and deconvolution of the core level of (b) C1s, (c) O1s, and (d) N 1 s spectra of TMB, Recycled TMB, and TMB/Rh B.

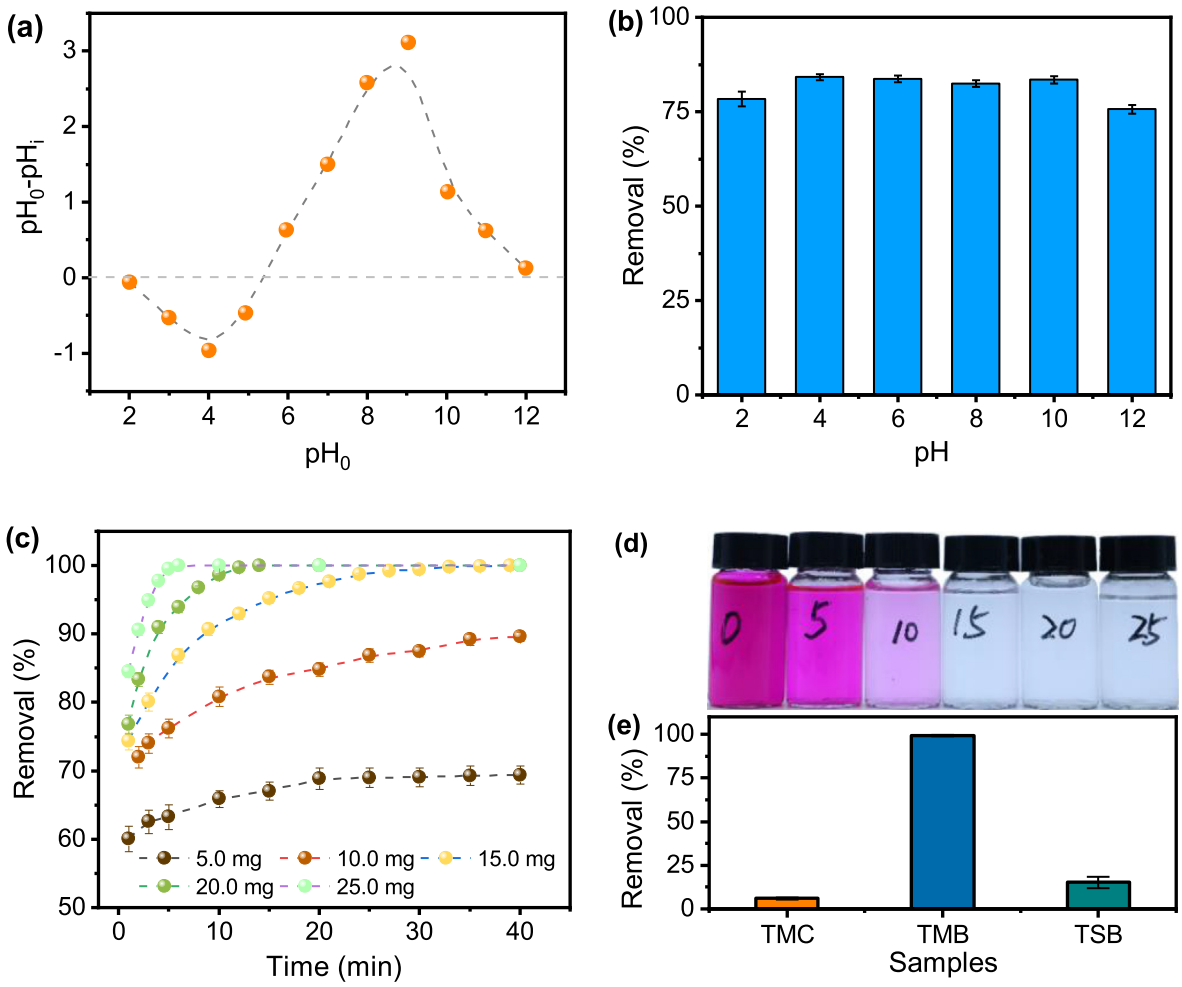

Fig. 4 (a) point of zero charges of TMB; (b) impact of pH medium on the removal of Rh B, TMB was 15.0 mg, the concentration of Rh B is 100.0 mg L^{-1}; (c) effect of TMB dosage on removal of Rh B against contact time, TMB was dispersed in 100.0 mL Rh B solution 100.0 mg L^{-1}, pH 3.7; (d) photograph taken at the time 40th min; (e) removal of TMB, TSB, and TMC; 15.0 mg biochar was dispersed in Rh B solution of 100.0 mg L^{-1}, pH 3.7.

removal didn't vary much because of the buffering effect of the adsorbent (Liu et al. 2012), the Rh B adsorption on biochar also involve other interactions, such as hydrogen bonding, pore filling, or π-π stacking besides electrostatic attraction. Even in strong acidic or basic conditions, the removal efficiency of Rh B is only about 5% lower than that at the optimal pH, implying that the as-prepared biochar is highly pH tolerant in the application. This phenomenon is consistent with much literature (Hou et al. 2011; Deng et al. 2019; Wu et al. 2020).

3.2.2. Effect of biochar dosage

As shown in Fig. 4(c, d), the removal improved from 67.9% to nearly 100% with an increasing dosage of TMB from 5.0 to 25.0 mg. This increase can be associated with the enhancement of available reaction sites for the adsorption, resulting in more dye being adsorbed from the solution. Therefore, the optimum amount of the adsorbent dosage required for dye removal is 15.0 mg which is much less than 80.0 mg (Xiao et al. 2020) and 100.0 mg (Wu et al. 2020) reported in the literature.

In addition, the removal efficiency of 15.0 mg TMC was only 6.0% under the same condition as shown in Fig. 4(e). For the comparative study, tobacco stem biochar (TSB) was prepared via a similar approach. However, its Rh B removal efficiency was found much lower, only about one-sixth adsorption capacity of TMB under similar conditions. SEM images of TSB showed it possessed much fewer *meso*-pores after pre-carbonization and activation (see Fig. 1(c, d)). While S_{BET} value of TSB (1734.0 m^2 g^{-1}) was closer to that of TMB (1841.9 m^2 g^{-1}). As seen in Fig. 2(a, b), the size of the hysteresis loop and pore size distribution were different in comparison with TMB. In Table 1, the average diameter of TMB is larger than TSB, which is beneficial for pore filling of dye molecules. The above-mentioned results indicate that two parts of tobacco behaved so differently in the dual-templating approach. This might be due to the different chemical compositions of the raw material (Table S1). For example, TM contains much less lignin and carbohydrates, while it possesses an excessive amount of hot water extractive agents compared with tobacco stem. Lignin has a high carbon content and thermally stability is better. Cellulose has a crystalline structure which is also beneficial for thermal stability. While the extracts in tobacco midrib account for more than 50%, mainly some small molecules such as nicotine, which are less stable. You

et al. also reported that biomass with high volatile matter contents could promote the development of porous structures (You et al. 2017). This is also evidenced by the different pyrolysis behaviors shown in Fig. S2.

3.3. Adsorption kinetics and isotherm

3.3.1. Adsorption kinetics

Fig. 5(a) displayed the adsorption behaviors of Rh B by TMB as a function of time. The adsorption process noticed rapid adsorption stages and slow adsorption stages. Thereafter, the removal reached 99.9% in 50.0 mg L^{-1} Rh B solution at 40th min. A higher removal rate at the early stage was ascribed to the ample amount of adsorption sites available on the TMB. As the adsorption proceeded, the adsorption rate was reduced. This might be due to the reduction of adsorption sites on TMB, and so did the concentration of Rh B (Wu et al. 2020). The results of the kinetics models fitted were shown in Fig. S3(a, b). All the parameters obtained from non-linear regression were listed in Table 2. It was observed that the adsorption was better described by the pseudo-second-order model than pseudo-second-order model according to the values of R^2. The values of all q_e obtained by non-linear fitting were smaller than the real adsorption capacities. The R^2 values of pseudo-first-order model R^2 were 0.9779 and 0.9273, respectively. The values of the K_1 and K_2 would reduce with the increase of C_0, indicating the adsorption rate induce as well. The R^2 of pseudo-second-order model was 0.9932 and 0.9716, indicating this model fit the adsorption data better enough, but it cannot conclude that the adsorption of adsorbate is via chemisorption [Tran, et al., 2017].

The initial dye concentration present in the solution and adsorption temperature would provide driving forces for the adsorption. As presented in Fig. 5(b), the equilibrium adsorption amount of Rh B increased with the increase of an initial dye concentration and adsorption temperature. The adsorption isotherm parameters obtained from linear regression were shown in Table 3. Langmuir model fitted the experimental data better according to the R^2 obtained from the Langmuir model was higher than those of Freundlich model, suggesting monolayer coverage of Rh B molecules onto the surface of TMB (Koltsakidou et al. 2021). The theoretical q_m at 25.0 and 55.0 °C fitted by the Langmuir isotherm model was 588.7 and 658.2 mg g^{-1}, respectively. While the q_m of TMC was about 20.0 mg g^{-1}, the adsorption capacity of TMB improved about 30 times compared to the adsorption capacity of TMC. The value of 1/n is < 1, indicating the favorable adsorption of Rh B with TMB (Yao et al. 2020).

Table 4 illustrates the comparison of q_m for Rh B dye adsorption as attained with some reported biochars or acti-

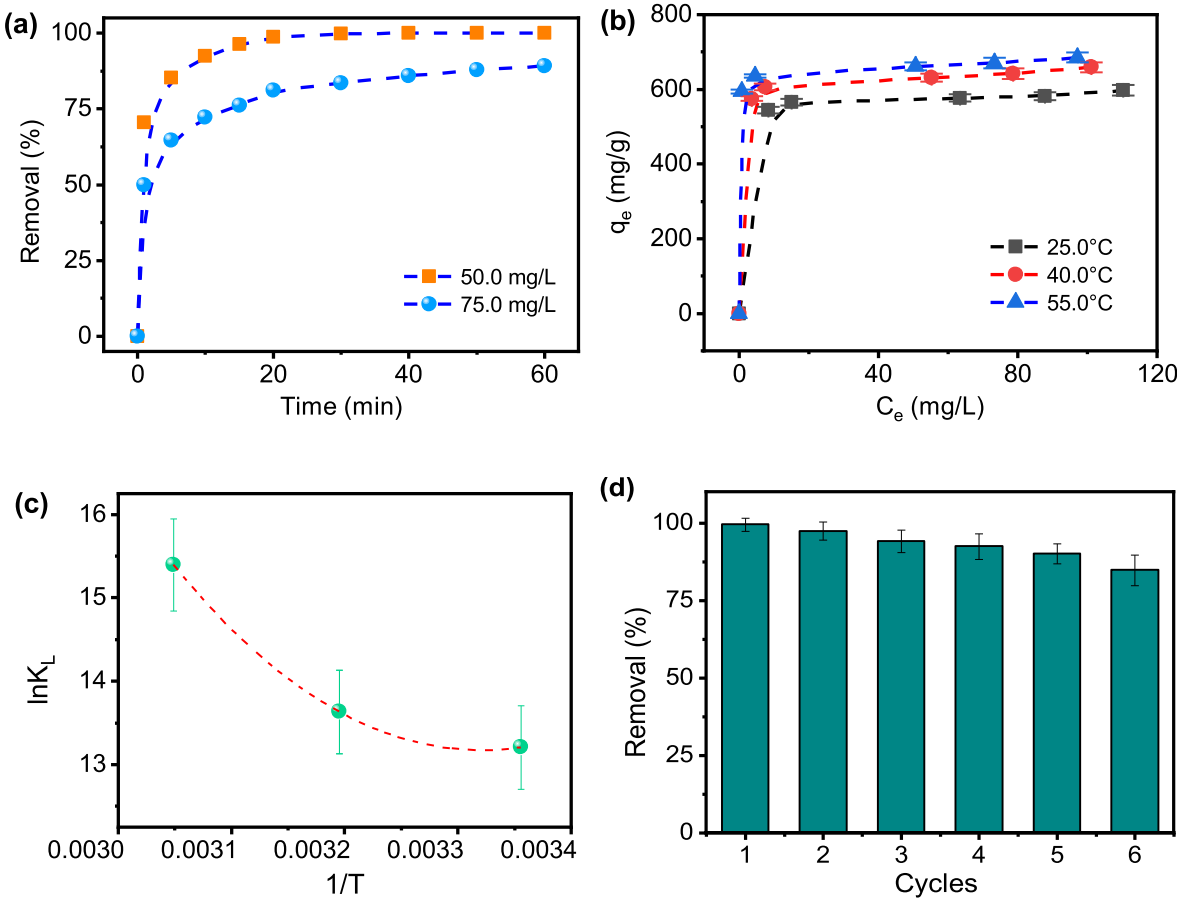

Fig. 5 (a) effect of contact time for Rh B adsorption on biochar (TMB is 15.0 mg, Temp. = 25.0 °C); (b) effect of temperature and concentration on Rh B removal using TMB; (c) lnK_L values as a function of 1/T for the observed rate constant for the adsorption onto TMB; (d) Rh B removal of TMB in 6 adsorption–desorption cycles (15.0 mg TMB, Rh B 100.0 mg L^{-1}, 25.0 °C).

Table 2 Parameters of kinetic models for Rh B removal.

C_0 (mg L^{-1})	Pseudo-first-order fitting			Pseudo-second-order fitting		
	R^2	K_1 (min^{-1})	q_e (mg g^{-1})	R^2	K_2 (g mg^{-1} min^{-1})	q_e (mg g^{-1})
50.0	0.9779	1.2962	322.0	0.9932	0.0065	332.0
75.0	0.9273	0.9121	401.6	0.9716	0.0026	425.7

Table 3 Parameters of isotherms models for Rh B adsorption.

Temp. (°C)	Langmuir isotherm model			Freundlich isotherm model		
	q_m (mg g^{-1})	$K_{L\ (L/mg)}$	R^2	K_F (mg^{1-n} g^{-1} L^n)	n^{-1}	R^2
25.0	588.7	1.48	0.9132	517.5	0.02769	0.8867
40.0	645.9	2.15	0.9582	553.3	0.03560	0.9299
55.0	658.2	9.70	0.8947	601.6	0.02794	0.9372

Table 4 Comparison of Rh B adsorption capacity in the literature under optimal conditions.

Adsorbent	q_m (mg/g)	Activator	Temperature (°C)	Heating rate (°/min)	Ref.
Tobacco midrib biochar	588.7	$K_2C_2O_4{\cdot}H_2O$, $CaCO_3$	800	3	This work
Tobacco stem biochar	98.1	$K_2C_2O_4{\cdot}H_2O$, $CaCO_3$	800	3	This work
Activated carbon derived from scrap tires	280.1	steam	800	none	(Li et al. 2010)
Activated carbon from bagasse pith	263.8	H_3PO_4	500	5	(Gad and El-Sayed 2009)
Cassava slag biochar	105.6	NaOH	700	none	(Xiao et al. 2020)
Bamboo shoot shell biochar	85.8	none	800	4	(Hou et al. 2019)
Plaintain peels biochar	84.4	$Fe(NO_3)_3$	750 ± 50 °C	none	(Adekola et al. 2019)

Gelatin/Activated carbon composite used commercial activated carbon.

vated carbon. The TMB obtained in the current work demonstrates much better performance than that described in the literature. Therefore, TMB obtained through a dual-templating approach is an excellent and promising adsorbent with a superior adsorption capacity toward Rh B dye.

3.3.2. Thermodynamic parameters

In Table 5, the negative value of ΔH^0 (–22.1 kJ mol^{-1}) revealed that the adsorption process of Rh B by TMB was exothermic, and the positive value of ΔS^0 (0.3 kJ mol^{-1}) demonstrated that the process of Rh B adsorption increased the disorder of the solid–liquid interface. Nevertheless, the contribution of entropy for the adsorption was insignificant as evidenced by the lower values of ΔS^0. As all ΔG^0 values are negative, it gave evidence that the adsorption was a spontaneous process in the tested temperature range. Furthermore, the ΔG^0 values (–33.3 ~ -41.6 kJ mol^{-1}) highlighted the role of electrostatic interaction between the adsorbed Rh B and TMB (Wu et al. 2020). Negative ΔC_p (-3.9 kJ mol^{-1} K^{-1}) indicated water molecules adsorbed on the biochar surface were replaced by dye molecules.

3.4. TMB regeneration

Moreover, the regeneration methodology will remove the dye molecules from the TMB surface effectively, thus allowing the used TMB to almost completely regain its original efficiency. Besides, from Fig. 2(d) and Fig. 3(d), both FT-IR spectra and XPS patterns show TMB and recycled TMB have almost similar characteristics, further confirming that Rh B is removed and surface groups retain after the regeneration treatment. In Fig. 5(d), the adsorption capacity of TMB decreased slightly during repeated use. The reason is that the dye adsorption process exists chemical adsorption, and the

Table 5 Thermodynamic parameters of Rh B adsorption.

Temp. (K)	ΔG^0 (kJ mol^{-1})	ΔH^0 (kJ mol^{-1})	ΔS^0 (kJ mol^{-1})	ΔC_p (kJ mol^{-1} K^{-1})
298	−33.3	−22.1	0.3	−3.9
313	−35.5			
328	−41.6			

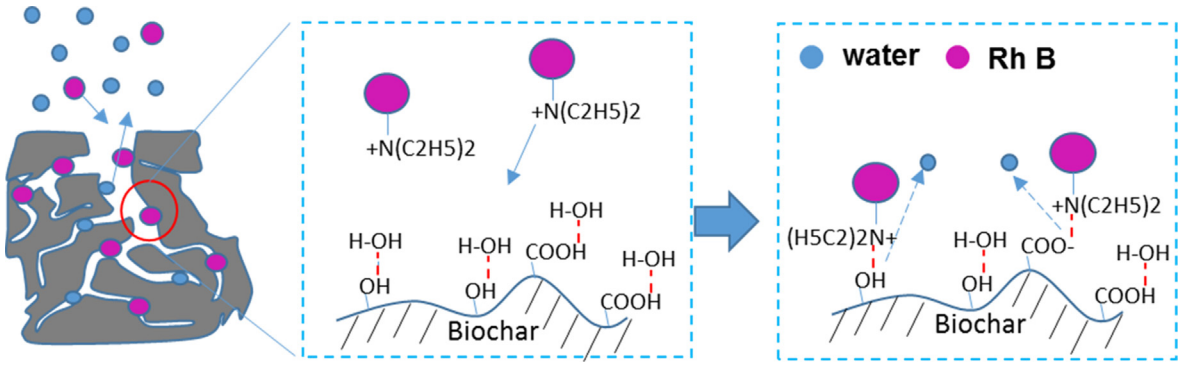

Fig. 6 Schematic representation of mechanism of Rh B adsorption on tobacco midrib biochar. (left) Hierarchically porous structure of biochar; (middle) scenario of Rh B and the surface chemistry of biochar; (right) Rh B adsorption on biochar driven by enthalpy and the new hydrogen bonding formation between Rh B and biochar, and release of water molecules. The Red dashed line represents hydrogen bonding.

adsorption capacity of TMB decreases due to the reduction of active sites during repeated use (Wang and Wang 2019).

3.5. Adsorption mechanisms of Rh B on TMB

The schematic representation of the mechanism of Rh B adsorption on biochar was illustrated in Fig. 6. From XPS (Fig. 3) and FT-IT spectra (Fig. 2(d)), the presence of carboxyl and hydroxyl groups on TMB enables the adsorbent to electrostatically assemble or form hydrogen bonding with the electronegative oxygen, nitrogen, and other non-covalent electron pairs in the adsorbed molecules. During Rh B adsorption, the electrostatic attraction between oppositely charged Rh B molecules and TMB surface forces the dye to be adsorbed on TMB. Meanwhile, the existing hydrogen bondings between water molecules and TMB surface are replaced by newly formed hydrogen bondings between Rh B and biochar. Therefore, water molecules are released. From FT-IR spectra (Fig. 2(d)), the presence of hydrogen bonding and the π-π interaction between the TMB and Rh B molecules was further confirmed by the stretching vibration peak of C-C groups of aromatic ring shifted from 1600 cm^{-1} for TMB to 1617 cm^{-1} for TMB/Rh B (Liu et al. 2019; Liu et al. 2021).

4. Conclusions

The results demonstrated that tobacco midrib was very suitable to produce biochar through a dual-templating approach. The prepared tobacco midrib-based biochar (TMB) possessed numerous meso-, micro-, and macro-pores and specific surface area reached 1841.9 m^2 g^{-1}. Such a unique porous structure enables it to be used as an efficient and promising adsorbent. The adsorption capacity of TMB towards Rhodamine B reached 588.7 mg/g. It could retain over 90% of the adsorption capacity after recycling 5 times. As indicated by the negative ΔG^0 and ΔH^0 values, the Rh B adsorption onto TMB was a spontaneous, and exothermic process. More importantly, negative ΔC_p (-3.9 kJ mol^{-1} K^{-1}) further confirmed that adsorbed water molecules on the biochar surface were replaced by dye molecules. This approach could effectively utilize the resources from tobacco waste and address the waste management-related environmental issues.

CRediT authorship contribution statement

Xinyu Zhang: Investigation, Visualization, Software, Writing – original draft. **Tingwei Zhang:** Conceptualization, Methodology, Writing – review & editing. **Jiaqi Guo:** Writing – review & editing. **Mehraj Ahmad:** . **Hui Yang:** Investigation. **Xiankun Su:** Investigation. **Feng Huang:** Resources. **Yongcan Jin:** Funding acquisition, Project administration. **Huining Xiao:** Supervision, Writing – review & editing. **Junlong Song:** Funding acquisition, Formal analysis, Writing – review & editing, Validation.

Acknowledgments

This work was supported by the National Natural Science Foundation of China (Nos. 31770623 and 31730106); Postgraduate Research & Practice Innovation Program of Jiangsu Province (SJKY19-0904); and the Priority Academic Program Development of Jiangsu Higher Education Institutions. The experimental assistance from the advanced analysis and test center of Nanjing Forestry University is gratefully acknowledged.

Appendix A. Supplementary data

Supplementary data to this article can be found online at https://doi.org/10.1016/j.arabjc.2022.103904.

References

Abdelhamid, H.N., Mathew, A.P., 2022. Cellulose–metal organic frameworks (CelloMOFs) hybrid materials and their multifaceted Applications: A review. Coord. Chem. Rev. 451,. https://doi.org/10.1016/j.ccr.2021.214263 214263.

Adekola, F.A., Ayodele, S.B., Inyinbor, A.A., 2019. Activated biochar prepared from plaintain peels: characterization and Rhodamine B adsorption data set. Chem. Data Collect. 19,. https://doi.org/10.1016/j.cdc.2018.11.012 100170.

Albadarin, A.B., Collins, M.N., Naushad, M., Shirazian, S., Walker, G., Mangwandi, C., 2017. Activated lignin-chitosan extruded blends for efficient adsorption of methylene blue. Chem. Eng. J. 307, 264–272. https://doi.org/10.1016/j.cej.2016.08.089.

Azari, A., Yeganeh, M., Gholami, M., Salari, M., 2021. The superior adsorption capacity of 2, 4-Dinitrophenol under ultrasound-

assisted magnetic adsorption system: Modeling and process optimization by central composite design. J. Hazard. Mater. 418,. https://doi.org/10.1016/j.jhazmat.2021.126348 126348.

Banozic, M., Aladic, K., Jerkovic, I., Jokic, S., 2020. Volatile organic compounds of tobacco leavesversuswaste (scrap, dust, and midrib): extraction and optimization. J. Sci. Food Agric. 101 (5), 1822–1832. https://doi.org/10.1002/jsfa.10796.

Bedin, K.C., Martins, A.C., Cazetta, A.L., Pezoti, O., Almeida, V.C., 2016. KOH-activated carbon prepared from sucrose spherical carbon: Adsorption equilibrium, kinetic and thermodynamic studies for Methylene Blue removal. Chem. Eng. J. 286, 476–484. https://doi.org/10.1016/j.cej.2015.10.099.

Boudissa, F., Mirilà, D., Arus, V.-A., Terkmani, T., Semaan, S., Proulx, M., Nistor, I.-D., Roy, R., Azzouz, A., 2019. Acid-treated clay catalysts for organic dye ozonation-Thorough mineralization through optimum catalyst basicity and hydrophilic character. J. Hazard. Mater. 364, 356–366. https://doi.org/10.1016/j.jhazmat.2018.09.070.

Crini, G., Lichtfouse, E., 2019. Advantages and disadvantages of techniques used for wastewater treatment. Environ. Chem. Lett. 17, 145–155. https://doi.org/10.1007/s10311-018-0785-9.

Deng, H., Mao, Z., Xu, H., Zhang, L., Zhong, Y., Sui, X., 2019. Synthesis of fibrous $LaFeO_3$ perovskite oxide for adsorption of Rhodamine B. Ecotoxicol. Environ. Safe. 168, 35–44. https://doi.org/10.1016/j.ecoenv.2018.09.056.

Gad, H.M.H., El-Sayed, A.A., 2009. Activated carbon from agricultural by-products for the removal of Rhodamine-B from aqueous solution. J. Hazard. Mater. 168, 1070–1081. https://doi.org/10.1016/j.jhazmat.2009.02.155.

Godiya, C.B., Ruotolo, L.A.M., Cai, W., 2020. Functional biobased hydrogels for the removal of aqueous hazardous pollutants: current status, challenges, and future perspectives. J. Mater. Chem. A 8, 21585–21612. https://doi.org/10.1039/D0TA07028A.

Gupta, H., Gupta, B., 2016. Adsorption of polycyclic aromatic hydrocarbons on banana peel activated carbon. Desalina. Water Treat. 57, 9498–9509. https://doi.org/10.1080/19443994.2015.1029007.

Hou, M.-F., Ma, C.-X., Zhang, W.-D., Tang, X.-Y., Fan, Y.-N., Wan, H.-F., 2011. Removal of rhodamine B using iron-pillared bentonite. J. Hazard. Mater. 186, 1118–1123. https://doi.org/10.1016/j.jhazmat.2010.11.110.

Hou, Y., Huang, G., Li, J., Yang, Q., Huang, S., Cai, J., 2019. Hydrothermal conversion of bamboo shoot shell to biochar: Preliminary studies of adsorption equilibrium and kinetics for rhodamine B removal. J. Anal. Appl. Pyrolysis 143,. https://doi.org/10.1016/j.jaap.2019.104694 104694.

Hu, B., Ai, Y., Jin, J., Hayat, T., Alsaedi, A., Zhuang, L., Wang, X., 2020. Efficient elimination of organic and inorganic pollutants by biochar and biochar-based materials. Biochar 2, 47–64. https://doi.org/10.1007/s42773-020-00044-4.

Hu, R.-S., Wang, J., Li, H., Ni, H., Chen, Y.-F., Zhang, Y.-W., Xiang, S.-P., Li, H.-H., 2015. Simultaneous extraction of nicotine and solanesol from waste tobacco materials by the column chromatographic extraction method and their separation and purification. Sep. Purif. Technol. 146, 1–7. https://doi.org/10.1016/j.seppur.2015.03.016.

Huang, Q., Song, S., Chen, Z., Hu, B., Chen, J., Wang, X., 2019. Biochar-based materials and their applications in removal of organic contaminants from wastewater: state-of-the-art review. Biochar 1, 45–73. https://doi.org/10.1007/s42773-019-00006-5.

Huang, Y., Huang, X., Ma, M., Hu, C., Seidi, F., Yin, S., Xiao, H., 2021. Recent advances on the bacterial cellulose-derived carbon aerogels. J. Mater. Chem. C 9, 818–828. https://doi.org/10.1039/D0TC05433J.

Jalili Naghan, D., Azari, A., Mirzaei, N., Velayati, A., Amini Tapouk, F., Adabi, S., Pirsaheb, M., Sharafi, K., 2015. Parameters effecting on photocatalytic degradation of the phenol from aqueous solutions in the presence of ZnO nanocatalyst under irradiation of UV-C light. Bulgarian Chemical Communications 47, 14–18.

Ji, Q., Li, H., 2021. High surface area activated carbon derived from chitin for efficient adsorption of Crystal Violet. Diam. Relat. Mater. 108516. https://doi.org/10.1016/j.diamond.2021.108516.

Jiang, T.-Y., Jiang, J., Xu, R.-K., Li, Z., 2012. Adsorption of Pb(II) on variable charge soils amended with rice-straw derived biochar. Chemosphere 89, 249–256. https://doi.org/10.1016/j.chemosphere.2012.04.028.

Jin, E., Guo, J., Yang, F., Zhu, Y., Song, J., Jin, Y., Rojas, O.J., 2016. On the polymorphic and morphological changes of cellulose nanocrystals (CNC-I) upon mercerization and conversion to CNC-II. Carbohydr. Polym. 143, 327–335. https://doi.org/10.1016/j.carbpol.2016.01.048.

Khan, M.A., Alqadami, A.A., Otero, M., Siddiqui, M.R., Alothman, Z.A., Alsohaimi, I., Rafatullah, M., Hamedelniel, A.E., 2019. Heteroatom-doped magnetic hydrochar to remove post-transition and transition metals from water: Synthesis, characterization, and adsorption studies. Chemosphere 218, 1089–1099. https://doi.org/10.1016/j.chemosphere.2018.11.210.

Koltsakidou, A., Terzopoulou, Z., Liakos, E.V., Evgenidou, E., Lambropoulou, D.A., Bikiaris, D.N., Kyzas, G.Z., 2021. Acrylic acid copolymers as adsorbent materials for the removal of anti-inflammatory pharmaceuticals from synthetic biomedical wastewaters. Colloid. Surf. A. 127382. https://doi.org/10.1016/j.colsurfa.2021.127382.

Landers, J., Gor, G.Y., Neimark, A.V., 2013. Density functional theory methods for characterization of porous materials. Colloid. Surf. A. 437, 3–32. https://doi.org/10.1016/j.colsurfa.2013.01.007.

Lee, D.-W., Jin, M.-H., Park, J.-H., Lee, Y.-J., Choi, Y.-C., 2018. Flexible synthetic strategies for lignin-derived hierarchically porous carbon materials. ACS Sustain. Chem. Eng. 6, 10454–10462. https://doi.org/10.1021/acssuschemeng.8b01811.

Li, B., Dai, F., Xiao, Q., Yang, L., Shen, J., Zhang, C., Cai, M., 2016. Nitrogen-doped activated carbon for a high energy hybrid supercapacitor. Energ. Environ. Sci. 9, 102–106. https://doi.org/10.1039/C5EE03149D.

Li, L., Liu, S., Zhu, T., 2010. Application of activated carbon derived from scrap tires for adsorption of Rhodamine B. J. Environ. Sci. 22, 1273–1280. https://doi.org/10.1016/S1001-0742(09)60250-3.

Li, Y., Xiao, H., Pan, Y., Zhang, M., Jin, Y., 2019. Thermal and pH dual-responsive cellulose microfilament spheres for dye removal in single and binary systems. J. Hazard. Mater. 377, 88–97. https://doi.org/10.1016/j.jhazmat.2019.05.033.

Liang, C., Li, Z., Dai, S., 2008. Mesoporous carbon materials: synthesis and modification. Angew. Chem. Int. Edit. 47, 3696–3717. https://doi.org/10.1002/anie.200702046.

Lin, R., Liang, Z., Yang, C., Zhao, Z., Cui, F., 2020. Selective adsorption of organic pigments on inorganically modified mesoporous biochar and its mechanism based on molecular structure. J. Colloid Interface Sci. 573, 21–30. https://doi.org/10.1016/j.jcis.2020.03.112.

Liu, H., Xu, G., Li, G., 2021. Preparation of porous biochar based on pharmaceutical sludge activated by NaOH and its application in the adsorption of tetracycline. J. Colloid Interface Sci. 587, 271–278. https://doi.org/10.1016/j.jcis.2020.12.014.

Liu, P., Liu, W.-J., Jiang, H., Chen, J.-J., Li, W.-W., Yu, H.-Q., 2012. Modification of bio-char derived from fast pyrolysis of biomass and its application in removal of tetracycline from aqueous solution. Bioresour. Technol. 121, 235–240. https://doi.org/10.1016/j.biortech.2012.06.085.

Liu, T., Zhang, Y., Lu, X., Wang, P., Zhang, X., Tian, J., Wang, Q., Song, J., Jin, Y., Xiao, H., 2020. Binding affinity of family 4 carbohydrate binding module on cellulose films of nanocrystals and nanofibrils. Carbohydr. Polym. 116725. https://doi.org/10.1016/j.carbpol.2020.116725.

Liu, X., Tian, J., Li, Y., Sun, N., Mi, S., Xie, Y., Chen, Z., 2019. Enhanced dyes adsorption from wastewater via Fe_3O_4 nanoparticles functionalized activated carbon. J. Hazard. Mater. 373, 397–407. https://doi.org/10.1016/j.jhazmat.2019.03.103.

Mena-Durán, C.J., Alonso-Lemus, I.L., Quintana, P., Barbosa, R., Ordoñez, L.C., Escobar, B., 2018. Preparation of metal-free electrocatalysts from cassava residues for the oxygen reduction reaction: A sulfur functionalization approach. Int. J. Hydrogen Energy 43, 3172–3179. https://doi.org/10.1016/j.ijhydene.2017.12.139.

Mudyawabikwa, B., Mungondori, H.H., Tichagwa, L., Katwire, D. M., 2017. Methylene blue removal using a low-cost activated carbon adsorbent from tobacco stems: kinetic and equilibrium studies. Water Sci. Technol. 75, 2390–2402. https://doi.org/10.2166/wst.2017.041.

Pariyar, P., Kumari, K., Jain, M.K., Jadhao, P.S., 2020. Evaluation of change in biochar properties derived from different feedstock and pyrolysis temperature for environmental and agricultural application. Sci. Total Environ. 713,. https://doi.org/10.1016/j.scitotenv.2019.136433 136433.

Paunovic, O., Pap, S., Maletic, S., Taggart, M.A., Boskovic, N., Sekulic, M.T., 2019. Ionisable emerging pharmaceutical adsorption onto microwave functionalised biochar derived from novel lignocellulosic waste biomass. J. Colloid Interface Sci. 547, 350–360. https://doi.org/10.1016/j.jcis.2019.04.011.

Pereira, M.F.R., Soares, S.F., Órfão, J.J.M., Figueiredo, J.L., 2003. Adsorption of dyes on activated carbons: influence of surface chemical groups. Carbon 41, 811–821. https://doi.org/10.1016/S0008-6223(02)00406-2.

Rattanachueskul, N., Saning, A., Kaowphong, S., Chumha, N., Chuenchom, L., 2017. Magnetic carbon composites with a hierarchical structure for adsorption of tetracycline, prepared from sugarcane bagasse via hydrothermal carbonization coupled with simple heat treatment process. Bioresour. Technol. 226, 164–172. https://doi.org/10.1016/j.biortech.2016.12.024.

Sevilla, M., Ferrero, G.A., Fuertes, A.B., 2017. One-pot synthesis of biomass-based hierarchical porous carbons with a large porosity development. Chem. Mater. 29, 6900–6907. https://doi.org/10.1021/acs.chemmater.7b02218.

Shi, Q., Zhang, X., Shen, B., Ren, K., Wang, Y., Luo, J., 2021. Enhanced elemental mercury removal via chlorine-based hierarchically porous biochar with $CaCO_3$ as template. Chem. Eng. J. 406,. https://doi.org/10.1016/j.cej.2020.126828 126828.

Soliman, A.I., Abdel-Wahab, A.-M.-A., Abdelhamid, H.N., 2022. Hierarchical porous zeolitic imidazolate frameworks (ZIF-8) and ZnO@N-doped carbon for selective adsorption and photocatalytic degradation of organic pollutants. RSC Adv. 12, 7075–7084. https://doi.org/10.1039/D2RA00503D.

Tang, R., Dai, C., Li, C., Liu, W., Gao, S., Wang, C., 2017. Removal of methylene blue from aqueous solution using agricultural residue walnut shell: equilibrium, kinetic, and thermodynamic studies. J. Chem. 2017. https://doi.org/10.1155/2017/8404965.

Tonucci, M.C., Gurgel, L.V.A., de Aquino, S.F., 2015. Activated carbons from agricultural byproducts (pine tree and coconut shell), coal, and carbon nanotubes as adsorbents for removal of sulfamethoxazole from spiked aqueous solutions: Kinetic and thermodynamic studies. Ind. crop. prod. 74, 111–121. https://doi.org/10.1016/j.indcrop.2015.05.003.

Wang, J., Wang, S., 2019. Preparation, modification and environmental application of biochar: A review. J. Clean. Prod. 227, 1002–1022. https://doi.org/10.1016/j.jclepro.2019.04.282.

Wang, Z., Shen, D., Shen, F., Wu, C., Gu, S., 2017. Kinetics, equilibrium and thermodynamics studies on biosorption of Rhodamine B from aqueous solution by earthworm manure derived biochar. Int. Biodeterior. Biodegrad. 120, 104–114. https://doi.org/10.1016/j.cej.2008.05.002.

Wei, D.W., Wei, H., Gauthier, A.C., Song, J., Jin, Y., Xiao, H., 2020. Superhydrophobic modification of cellulose and cotton textiles: methodologies and applications. J. Bioresour. Bioprod. 5, 1–15. https://doi.org/10.1016/j.jobab.2020.03.001.

Wu, J., Yang, J., Huang, G., Xu, C., Lin, B., 2020. Hydrothermal carbonization synthesis of cassava slag biochar with excellent adsorption performance for Rhodamine B. J. Clean. Prod. 251,. https://doi.org/10.1016/j.jclepro.2019.119717 119717.

Wu, W., Mei, Y., Zhang, L., Liu, R., Cai, J., 2015. Kinetics and reaction chemistry of pyrolysis and combustion of tobacco waste. Fuel 156, 71–80. https://doi.org/10.1016/j.fuel.2015.04.016.

Xiang, W., Zhang, X., Chen, J., Zou, W., He, F., Hu, X., Tsang, D.C. W., Ok, Y.S., Gao, B., 2020. Biochar technology in wastewater treatment: A critical review. Chemosphere 252,. https://doi.org/10.1016/j.chemosphere.2020.126539 126539.

Xiao, W., Garba, Z.N., Sun, S., Lawan, I., Wang, L., Lin, M., Yuan, Z., 2020. Preparation and evaluation of an effective activated carbon from white sugar for the adsorption of rhodamine B dye. J. Clean. Prod. 253,. https://doi.org/10.1016/j.jclepro.2020.119989 119989.

Xu, Z., Huang, Y., Ding, L., Huang, J., Gao, H., Li, T., 2020. Highly stable basswood porous carbon anode activated by phosphoric acid for a sodium ion battery. Energ. Fuel. 34, 11565–11573. https://doi.org/10.1021/acs.energyfuels.0c02286.

Yao, X., Ji, L., Guo, J., Ge, S., Lu, W., Cai, L., Wang, Y., Song, W., Zhang, H., 2020. Magnetic activated biochar nanocomposites derived from wakame and its application in methylene blue adsorption. Bioresour. Technol. 302,. https://doi.org/10.1016/j.biortech.2020.122842 122842.

You, S., Ok, Y.S., Chen, S.S., Tsang, D.C.W., Kwon, E.E., Lee, J., Wang, C.-H., 2017. A critical review on sustainable biochar system through gasification: Energy and environmental applications. Bioresour. Technol. 246, 242–253. https://doi.org/10.1016/j.biortech.2017.06.177.

Zhang, J., Shao, J., Jin, Q., Li, Z., Zhang, X., Chen, Y., Zhang, S., Chen, H., 2019. Sludge-based biochar activation to enhance Pb(II) adsorption. Fuel 252, 101–108. https://doi.org/10.1016/j.fuel.2019.04.096.

Zhang, X., Tian, J., Wang, P., Liu, T., Ahmad, M., Zhang, T., Guo, J., Xiao, H., Song, J., 2022. Highly-efficient nitrogen self-doped biochar for versatile dyes' removal prepared from soybean cake via a simple dual-templating approach and associated thermodynamics. J. Clean. Prod. 332,. https://doi.org/10.1016/j.jclepro.2021.130069 130069.

Zhou, Z., Xu, Z., Feng, Q., Yao, D., Yu, J., Wang, D., Lv, S., Liu, Y., Zhou, N., Zhong, M.-E., 2018. Effect of pyrolysis condition on the adsorption mechanism of lead, cadmium and copper on tobacco stem biochar. J. Clean. Prod. 187, 996–1005. https://doi.org/10.1016/j.jclepro.2018.03.268.